Holoscopy – Holographic optical coherence tomography

Dierck Hillmann[a,b], Christian Lührs[a,c], Tim Bonin[c], Peter Koch[a], Alfred Vogel[c], Gereon Hüttmann[b,c]

[a]Thorlabs GmbH, Maria-Goeppert-Str. 1, 23562 Lübeck, Germany
[b]Medizinisches Laserzentrum Lübeck, Peter-Monnik-Weg 4, 23562 Lübeck, Germany
[c]Institut für Biomedizinische Optik, Peter-Monnik-Weg 4, 23562 Lübeck, Germany

ABSTRACT

We demonstrate Holoscopy – a combination of full-field swept-source optical coherence tomography and digital holography. By using a simple Michelson interferometer setup, a rapidly tunable laser and combining scalar diffraction theory with standard Fourier-domain OCT signal processing we obtain depth invariant imaging quality.

1. INTRODUCTION

In scanning Fourier-domain optical coherence tomography (FD-OCT) confocal detection of light backscattered from a sample is used and combined with additional depth discrimination introduced by the coherence gate. Although the depth resolution in FD-OCT is independent of the confocal gating and not limited by the Rayleigh length, imaging with a high NA is hardly possible, as the confocal gating still rejects photons outside the focus region. Going to higher NA further increases the lateral resolution and the amount of light detected from the focus region but also limits the depth of focus and thus further decreases imaging quality with respect to sensitivity and resolution in other layers (fig. 1).

Several solutions have been proposed to overcome the classical Rayleigh limit of Gaussian optics. Inverse scattering and holographic techniques can increase the lateral resolution of scanning FD-OCT,[1–3] however the rejection of photons due to the confocal gating is still present and thus imaging quality still degrades for out-of-focus regions. On the other hand, Fourier-domain full-field OCT[4,5] and first attempts to combine Digital Holography (DH) with FD-OCT[6,7] have been demonstrated and remove the confocal gating however resolution is still not depth invariant. Finally, Digital Interference Holography[8] basically provides three-dimensional tomographic images with depth invariant resolution by using several wavelengths. However, compared to FD-OCT these images show poor quality and the numerical reconstruction is very expensive.

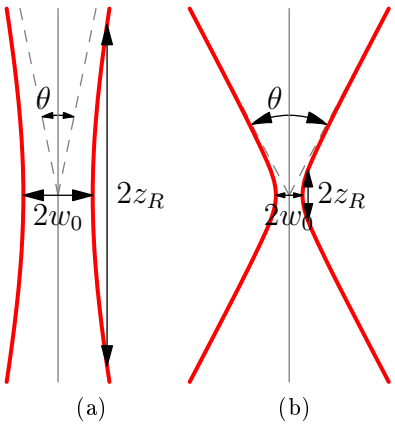

Figure 1: Schematic representation of a Gaussian beam for a low Numerical Aperture (a) and a high Numerical Aperture (b). Going to high NA the detection angle θ and the lateral resolution presented by the beam width $2w_0$ improve, while the possible measurement depth indicated by the Rayleigh length $2z_R$ decreases.

Optical Coherence Tomography and Coherence Techniques V, edited by Rainer A. Leitgeb, Brett E. Bouma, Proc. of SPIE-OSA Biomedical Optics, SPIE Vol. 8091, 80911H

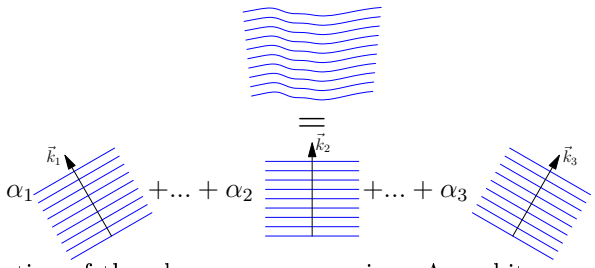

Figure 2: Schematic representation of the plane wave expansion. An arbitrary wave field (top) can be mathematically decomposed in a superposition of plane waves (bottom), where each wave has a different amplitude, phase (represented by $\alpha_i \in \mathbb{C}$) and direction (represented by $\vec{k}_i$).

2. DIGITAL HOLOGRAPHY

Digital Holography is an interferometric technique and as such uses setups similar to OCT. Spatial and temporal coherent light is reflected from a sample and together with reference light brought onto an area detector, for example a CMOS-camera. The intensity on the detector is given by

$$I(x,y) \propto |R(x,y) + S(x,y)|^2 = |R(x,y)|^2 + |S(x,y)|^2 + 2\mathrm{Re}\left(R^* S\right)(x,y),$$

where $S(x,y)$ is the sample field in the detector plane and $R(x,y)$ is the known reference field in the detector plane. Using the knowledge of the reference field $R(x,y)$ the sample field $S(x,y)$ can be computed – albeit disturbed by the DC Terms $|R|^2 + |S|^2$ and a complex conjugated component, which are reduced by techniques known in DH[9,10] or neglected, respectively.

2.1 Propagation of the wave field

Knowing a complex wave field in one plane it can be propagated numerically to any other plane parallel to the original one. There are several methods to achieve this, for example a Fresnel transform can be used if the planes are sufficiently far away for this approximation to be valid or the complete diffraction integral can be solved, however this is numerically expensive. An alternative is to compute the angular spectrum of the wave field: Each complex wave field in a given plane can be represented as a superposition of plane waves as illustrated in fig. 2, where the amplitude, phase and direction of these plane waves will vary. Without loss of generality we can assume that the wave originally is given in the plane $z = 0$. The decomposition can be computed by a two-dimensional Fourier transform, the amplitude and phase of the wave with lateral components k_x and k_y are thus given by

$$\tilde{S}(k_x, k_y, z=0) = \mathcal{F}_{x,y \to k_x, k_y}\left[S(x,y,z=0)\right] = \frac{1}{2\pi} \iint_{\mathbb{R}^2} \mathrm{d}x\, \mathrm{d}y\, S(x,y,z=0)\, \mathrm{e}^{-\mathrm{i}(k_x x + k_y y)}.$$

For these plane waves the lateral components k_x and k_y of the wave vector are given, where $\hat{e}_z$ is direction perpendicular to the original data-plane. If additionally the complete length $||\vec{k}|| = k$ of the wave vector $\vec{k}$ is known the complete wave vector can be computed and is given by

$$\vec{k} = \begin{pmatrix} k_x \\ k_y \\ k_z \end{pmatrix} = \begin{pmatrix} k_x \\ k_y \\ \sqrt{k^2 - k_x^2 - k_y^2} \end{pmatrix}.$$

Each of these plane waves building the wave field can now be propagated independently as their wave vector is known completely. A plane wave will be a plane wave in all planes, only its phase is going to change. If propagated from plane $z = 0$ to plane $z = \Delta z$ the phase of the plane wave is going to change according to

$$\tilde{S}(k_x, k_y, z=\Delta z) = \mathrm{e}^{-\mathrm{i}k_z \Delta z} S(k_x, k_y, z=0)$$

as illustrated in fig. 3.

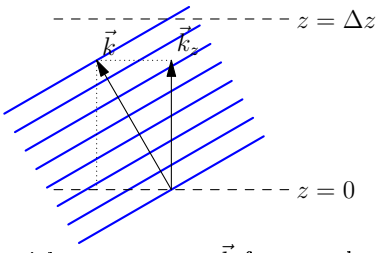

Figure 3: Propagation of a plane wave with wave vector $\vec{k}$ from a plane $z = 0$ to a plane $z = \Delta z$. The plane wave will only gain an additional phase factor in the resulting plane which is given by $\exp(-\mathrm{i}k_z\Delta z)$.

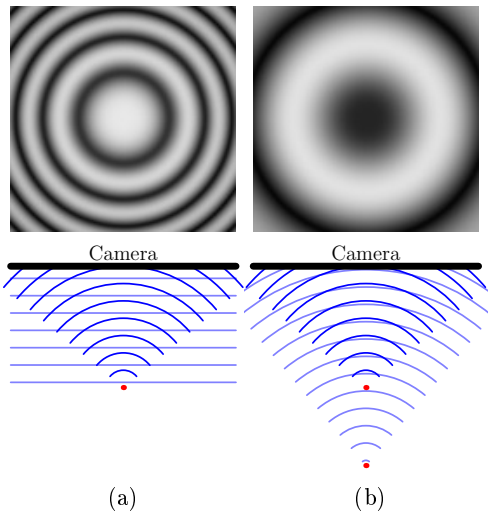

Figure 4: Schematic representation of the spatial interference fringes when using a parallel reference wave (a) and a spherical reference wave (b). The spatial frequencies of the interference fringes are significantly lower if a spherical reference wave is used and thus the requirements on the resolution of the camera is reduced.

By simply inverse Fourier transforming the propagated complex amplitudes $\tilde{S}(k_x, k_y, z = \Delta z)$, the wave field in the new plane $z = \Delta z$ can be computed:

$$S(x, y, z = \Delta z) = \mathcal{F}^{-1}_{k_x,k_y \to x,y}\left[\tilde{S}(k_x, k_y, z = \Delta z)\right] = \frac{1}{2\pi}\iint_{\mathbb{R}^2} \mathrm{d}k_x\,\mathrm{d}k_y\,\tilde{S}(k_x, k_y, z = \Delta z)\,\mathrm{e}^{+\mathrm{i}(k_x x + k_y y)}$$

If the reconstruction plane $z = \Delta z$ is chosen in the sample, the structures there will be imaged sharply as if they were focused using classical imaging systems.

2.2 The sampling problem

It is important to note that the lateral interference fringes of the intensity distribution $I(x, y)$ that occur in the camera plane need to be resolved by the digital camera. Otherwise under-sampled signals lead to imaging artifacts and twin images of the imaged structures. However, the spatial frequency of these interference fringes increases if the sample is put closer to the camera plane and as such there is a minimal distance $z_{\min}$ between sample and camera. The solid angle of backscattered light that is detected determines the sensitivity and maximal resolution of the imaging system analogous to the Numerical Aperture (NA) in classical imaging systems. This angle can most easily be increased by putting the sample closer to the camera and thus choosing the reference plane $z = z_{\mathrm{ref}}$ to be identical to the minimal sample distance $z = z_{\min} = z_{\mathrm{ref}}$. Additionally the minimal distance can be decreased by choosing a spherical reference wave instead of a collimated reference wave as illustrated in fig. 4. This way an optimal geometrical setup for lens-less imaging with respect to resolution and sensitivity can be found.

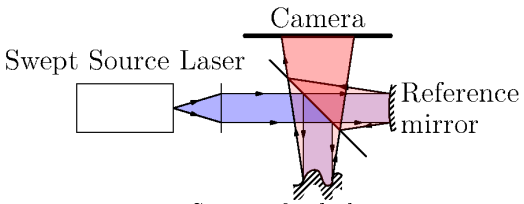

Figure 5: Setup of a holoscope.

3. SETUP

The simple Michelson interferometer setup is illustrated in fig. 5. The collimated reference beam is split in sample and reference arm. The sample beam illuminates the sample and the backscattered light is brought onto the camera. The reference beam is widened using a convex reference mirror with $f = -10.34\,\mathrm{mm}$ and superimposed with the sample beam on the CMOS-camera. Two different cameras were used, depending on the required speed. For *ex-vivo* measurements a Mikrotron EoSens MC3010 was used which can image 1024×1024 pixels of size $8\,\mu\mathrm{m} \times 8\,\mu\mathrm{m}$ with up to 630 fps. For *in-vivo* measurements a Photron FASTCAM SA5 was used that can image 1024×1024 pixels of size $20\,\mu\mathrm{m} \times 20\,\mu\mathrm{m}$ with 7000 fps. The tunable laser was a Superlum Broadsweeper BS-840-01, sweeping from 873.5 nm to 823.5 nm, its sweep rate was adjusted to the frame rate of the respective camera to give 1024 frames for different wave numbers k during one sweep. Camera and light source were hardware synced. The distance of the camera plane to the sample was adjusted to 8 cm for *ex-vivo* measurements and 14 cm for *in-vivo* measurements, corresponding to NAs of 0.05 and 0.07, respectively.

Using this setup the axial resolution of the holoscopic imaging is $14.7\,\mu\mathrm{m}$ after Hann-shaping of the spectra, with a full measurement depth of 3.8 mm. The lateral resolution was $2w_0 = 7\,\mu\mathrm{m}$ for *in-vivo* measurements and $2w_0 = 11\,\mu\mathrm{m}$ for *ex-vivo* measurements and the corresponding Rayleigh lengths were $2z_R = 100\,\mu\mathrm{m}$ and $2z_R = 200\,\mu\mathrm{m}$, respectively.

4. DATA RECONSTRUCTION

Data was reconstructed by propagating all holograms to a common plane $z = z''$ inside the sample. Afterwards standard Fourier-domain OCT processing techniques could be applied in order to give a depth resolved image, which thus gives the scattering of the sample $S(x, y, z_{\mathrm{ref}} + z')$, where $z = z_{\mathrm{ref}}$ is the reference plane. However, lateral resolution will only be optimal in the plane $z = z''$ chosen as reconstruction distance. This reconstruction is thus given by

$$S(x, y, z_{\mathrm{ref}} + z') \propto \int_{\mathbb{R}} \mathrm{d}k\, \mathrm{e}^{-\mathrm{i}2kz'} \mathcal{F}^{-1}_{k_x,k_y \to x,y} \left[\mathrm{e}^{-\mathrm{i}z''\sqrt{k^2 - k_x^2 - k_y^2}} \mathrm{e}^{+\mathrm{i}kz''} \mathcal{F}_{x,y \to k_x,k_y} \left[S(x, y, z = 0; k) \right] \right], \qquad (1)$$

where $S(x, y, z_{\mathrm{ref}} + z')$ is the reconstructed complex scattering amplitude, $S(x, y, z = 0; k)$ is the sample wave field in the camera plane acquired with the wavenumber k and $\mathcal{F}_{x,y \to k_x,k_y}$ is the two-dimensional Fourier transform along the x- and y-axis and $\mathcal{F}^{-1}_{k_x,k_y \to x,y}$ its inverse. The additional phase factor $\mathrm{e}^{+\mathrm{i}kz'}$ has been introduced to compensate for the numerical optical path length introduced by the propagation of the wave field. It is required to maintain the phase-encoded depth information as used by the FD-OCT part. Additionally, it is important to note that the wave field in the camera plane $S(x, y, z = 0; k)$ needs to be computed without changing the phase of the signal, i. e. for at least one data point $(x, y) = (x_0, y_0)$ the reference field $R(x, y; k)$ should be constant and independent of the wavenumber k.

As the same raw data can be used to reconstruct for several layers $z = z''$, the reconstruction can also be performed for all depths. This means that the outlined reconstruction can be used to gain depth independent lateral resolution by stitching together datasets for different numerical reconstruction distances.

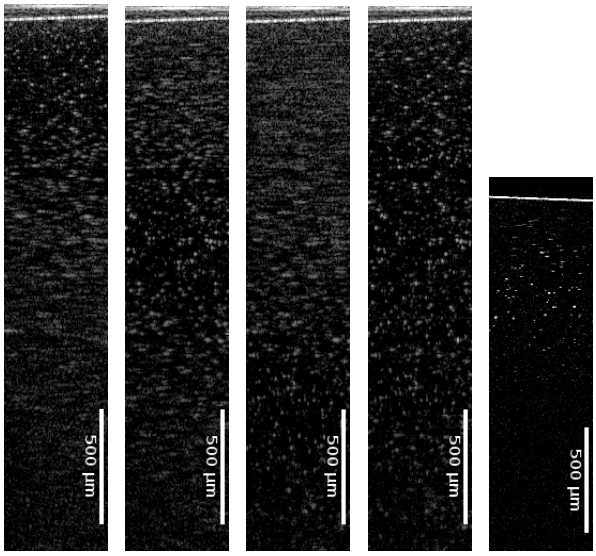

(a) (b) (c) (d) (e)

Figure 6: Comparison of holoscopic B-scans of a scattering sample (a)-(d) with B-scans of a standard spectrometer-based FD-OCT (e). Single reconstructions of the holoscopy data have been performed for various layers (a)-(c) and a B-scan stiched together of five single reconstructions is shown in (d). The holoscopy measurements correspond to an NA of 0.05, the standard FD-OCT measurements were using an NA of 0.06.

4.1 Reconstruction performance

The suggested reconstruction (1) is numerically expensive compared to standard FD-OCT processing. A single reconstruction of a volume of $1024 \times 1024 \times 512$ voxels (approximately 1 mio A-scans) takes about 22 s on a Quad CPU Opteron 6180 with 48 cores. Additionally, there are large requirements on the RAM in order to keep all required data in memory and not cache to disk. The complete unprocessed dataset after computing the sample wave field gets as large as $1024 \times 1024 \times 1024$ complex single-precision floating point numbers (i. e. 2×4 bytes per complex number). Therefore at least 8 GBytes of memory are required.

5. RESULTS

We demonstrated the depth independent resolution and sensitivity by using a scattering phantom which is build from polyurethane resin doped with a low density of $300 - 800$ nm sized red iron oxide nanoparticles[11] and compared it to a standard spectrometer-based FD-OCT using a Basler Runner ruL2048gm camera and an SLD with a central wavelength of 910 nm, an axial resolution of 5.4 μm in air and a full measurement depth of 2.7 mm. It can be seen, that the standard FD-OCT image in fig. 6e is degrading outside the focus with respect to sensitivity and resolution. A few hundred micrometers outside the focus layer no scatterers can be seen and basically no imaging is possible for this sample. For the single reconstructed holoscopic tomography in fig. 6a-6c however the scatterers can be seen over the complete measurement depth and only the resolution degrades outside the chosen reconstruction distance. Finally, the holoscopic reconstruction shown in fig. 6d has been stitched together of five single reconstructions and shows scatterers with the same resolution over the complete measurement depth.

Additionally we demonstrated *in-vivo* imaging by measuring a finger tip that was stabilized by a glass plate using the Photron FASTCAM SA5. The resulting tomographies are shown in fig. 7. Features known from standard FD-OCT imaging such as the perspiratory glands and the stratus corneum are visible.

Finally, an *ex-vivo* measurements of a grape is shown in fig. 8. The cell structure can clearly be recognized and imaging quality is comparable to a standard 2D-scanning FD-OCT images.

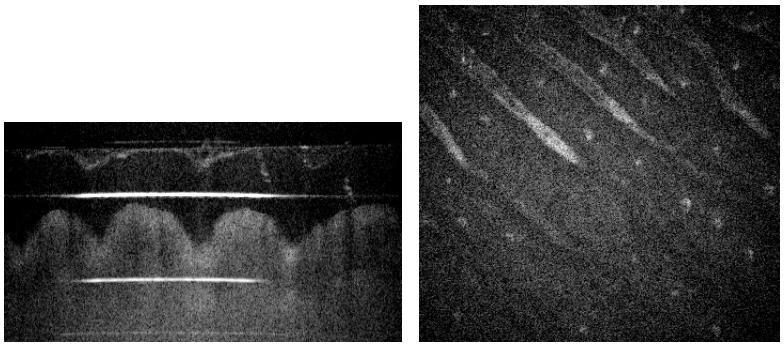

(a) (b)

Figure 7: Holoscopic *in-vivo* images of a finger tip. The B-scan (a) and the en-face image (b) show structures familiar from standard FD-OCT imaging and for example perspiratory glands are clearly visible.

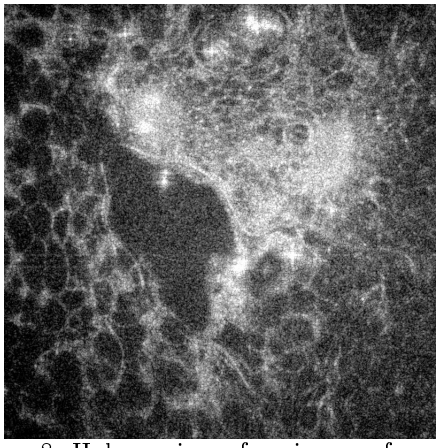

Figure 8: Holoscopic en-face image of grape.

5.1 Limitations

Although the presented holoscopic images show features similar to standard FD-OCT they also are more sensitive to artifacts. Due to multiple scattering of photons structures from depths are visible where no physical structures are present, while for standard FD-OCT the confocal gating often rejects these multiple scattered photons. The lateral position of these structures can mostly be reconstructed by the holographic technique however the multiple scattering introduces additional path lengths and thus the OCT part reconstructs these structures to a higher depth introducing shadows in the images. Additionally, reflecting surfaces in the setup can lead to horizontal lines in the image, however these can be eliminated, for example by using suitable optics.

A further problem of the presented approach appears for *in-vivo* imaging where the motion of the sample is inevitable. Contrary to scanning OCT the fast axis is no longer the z-axis and the acquisition time of the complete volume and single A-scan are identical for holoscopy. This leads to increased sensitivity for motion induced artifacts and therefore makes *in-vivo* applications more complicated as high-speed cameras are required.

6. CONCLUSION AND OUTLOOK

We demonstrated holoscopy and combined holographic techniques with Fourier-domain OCT. With this combination we achieved a depth-invariant imaging quality with respect to sensitivity and lateral resolution and were able to overcome the classical limits imposed by the Rayleigh length, as present in optical imaging systems. Although this technique still shows problems with respect to imaging artifacts its full advantage will only be visible when going to higher resolutions. In principle the origin of all single scattered photons can be reconstructed and no photons are rejected as in time-domain OCT, optical coherence microscopy or confocal microscopy. If the

imaging depth becomes significantly larger than the Rayleigh length corresponding to the lateral resolution it provides thus the possibility to measure more effectively than other imaging techniques.

The next step is therefore to go to higher imaging NAs and higher axial resolution and to obtain imaging quality with an almost isotropic resolution in the region of a single micron. As such holoscopy has the potential to provide optical biopsy with resolutions comparable to the microscopic imaging of histologies.

REFERENCES

[1] Ralston, T. S., Marks, D. L., Scott Carney, P., and Boppart, S. A., "Interferometric synthetic aperture microscopy," *Nat Phys* **3**(2), 129–134 (2007). 10.1038/nphys514.

[2] Ralston, T. S., Marks, D. L., Carney, P. S., and Boppart, S. A., "Real-time interferometric synthetic aperture microscopy," *Opt Express* **16**(4), 2555–69 (2008).

[3] Yu, L., Rao, B., Zhang, J., Su, J., Wang, Q., Guo, S., and Chen, Z., "Improved lateral resolution in optical coherence tomography by digital focusing using two-dimensional numerical diffraction method," *Opt. Express* **15**(12), 7634–7641 (2007).

[4] Považay, B., Unterhuber, A., Hermann, B., Sattmann, H., Arthaber, H., and Drexler, W., "Full-field time-encoded frequency-domain optical coherence tomography," *Opt. Express* **14**(17), 7661–7669 (2006).

[5] Bonin, T., Franke, G., Hagen-Eggert, M., Koch, P., and Hüttmann, G., "In vivo fourier-domain full-field oct of the human retina with 1.5 million a-lines/s," *Opt. Lett.* **35**(20), 3432–3434 (2010).

[6] Zvyagin, A. V. and et al., "Image reconstruction in full-field fourier-domain optical coherence tomography," *Journal of Optics A: Pure and Applied Optics* **7**(7), 350 (2005).

[7] Shabanov, D. V., Geliknov, G. V., and Gelikonov, V. M., "Broadband digital holographic technique of optical coherence tomography for 3-dimensional biotissue visualization," *Laser Physics Letters* **6**(10), 753–758 (2009).

[8] Potcoava, M. C. and Kim, M. K., "Optical tomography for biomedical applications by digital interference holography," *Measurement Science and Technology* **19**(7), 074010 (2008).

[9] Kim, M. K., "Principles and techniques of digital holographic microscopy," *SPIE Reviews* **1**(1), 018005 (2010).

[10] Schnars, U. and Jüptner, W. P. O., "Digital recording and numerical reconstruction of holograms," *Measurement Science and Technology* **13**(9), R85 (2002).

[11] Woolliams, P. D., Ferguson, R. A., Hart, C., Grimwood, A., and Tomlins, P. H., "Spatially deconvolved optical coherence tomography," *Appl Opt* **49**(11), 2014–21 (2010).